Gas diffusion through columnar laboratory sea ice: implications for mixed-layer ventilation of CO_2 in the seasonal ice zone

By B. LOOSE[1,2,3]*, P. SCHLOSSER[1,2,4], D. PEROVICH[5], D. RINGELBERG[5], D.T. HO[6], T. TAKAHASHI[1,2], J. RICHTER-MENGE[5], C.M. REYNOLDS[5], W.R. MCGILLIS[1,4] and J.-L. TISON[7], [1]*Lamont-Doherty Earth Observatory of Columbia University, 61 Route 9W, Palisades, NY 10964, USA;* [2]*Department of Earth and Environmental Sciences, Columbia University, Room 106 Geoscience Building, Palisades, NY 10964, USA;* [3]*Department of Marine Chemistry and Geochemistry, Woods Hole Oceanographic Institution, Woods Hole, MA 02543, USA;* [4]*Department of Earth and Environmental Engineering, Columbia University, 918 Seeley Mudd Building, Columbia University, 500 West 120th Street, New York, NY 10027, USA;* [5]*US Army Corps of Engineers Cold Regions Research and Engineering Laboratory, 72 Lyme Road, Hanover, NH 03755, USA;* [6]*Department of Oceanography, University of Hawai'i at Manoa, 1000 Pope Road, Honolulu, HI 96822, USA;* [7]*Laboratoire de Glaciologie, Université Libre de Bruxelles. 50, Avenue F.D. Roosevelt, 1050 Bruxelles, Belgium*

(Manuscript received 30 June 2009; in final form 12 August 2010)

ABSTRACT

Gas diffusion through the porous microstructure of sea ice represents a pathway for ocean–atmosphere exchange and for transport of biogenic gases produced within sea ice. We report on the experimental determination of the bulk gas diffusion coefficients, D, for oxygen (O_2) and sulphur hexafluoride (SF_6) through columnar sea ice under constant ice thickness conditions for ice surface temperatures between -4 and $-12\,°C$. Profiles of SF_6 through the ice indicate decreasing gas concentration from the ice/water interface to the ice/air interface, with evidence for solubility partitioning between gas-filled and liquid-filled pore spaces. On average, D_{SF_6} was 1.3×10^{-4} cm^2 s^{-1} ($\pm 40\%$) and D_{O_2} was 3.9×10^{-5} cm^2 s^{-1} ($\pm 41\%$). The preferential partitioning of SF_6 to the gas phase, which is the dominant diffusion pathway produced the greater rate of SF_6 diffusion. Comparing these estimates of D with an existing estimate of the air–sea gas transfer through leads indicates that ventilation of the mixed layer by diffusion through sea ice may be negligible, compared to air–sea gas exchange through fractures in the ice pack, even when the fraction of open water is less than 1%.

1. Introduction

The maximum areal extent of Antarctic sea ice during austral winter is about 18 million km^2 (based on the 40-year average from the National Snow and Ice Data centre), which represents 39% of the ocean surface south of 50°S. It presents a significant barrier to ventilation of the underlying water column. This maximum in sea ice cover occurs at a time when the mixed layer has reached its greatest depth and when the density stratification of the Southern Ocean is least resistant to exchange with the atmosphere. The combination of these asynchronous barriers to gas transport determines the net physical flux of inorganic carbon, among other gases, between the atmosphere and the ocean

mixed layer, and may also be important to exchange between the atmosphere and the abyssal ocean. In the Southern Ocean, the mean air–sea CO_2 partial pressure difference (ΔpCO_2) builds up to ca. 40 μatm beneath sea ice (Takahashi et al., 2009), establishing a thermodynamic gradient that favours CO_2 evasion from the mixed layer. Yet, the pathways and rates of air–sea gas exchange in the presence of sea ice cover are not yet well established.

When the temperature in sea ice decreases below the freezing point of seawater (e.g. $< -1.8\,°C$), $CaCO_3$ precipitation in brine can increase the partial pressure of CO_2 (pCO_2) within the ice microstructure (Papadimitriou et al., 2003). Depending on the gas permeability of winter sea ice, this CO_2 may evade the brine and diffuse to the atmosphere. Conversely, algal blooms in sea ice have been observed coincident with low pCO_2 in brine and with measurable fluxes of O_2 and dimethylsuphide (DMS) from the ice to the atmosphere (Delille et al., 2007). The

magnitude of each of these processes and their net effect on the Southern Ocean carbon budget has not been established, and they depend directly on the rate of gas transport through sea ice.

The first published measurements of the rate of bulk gas diffusion D through sea ice were conducted by Gosink et al. (1976), who measured gas migration through pack ice northeast of Barrow, Alaska. Their results ranged from $D = 10^{-7}$ to 10^{-5} cm^2 s^{-1} atm^{-1}, depending on the temperature and the gas compound in question. In this study, we have performed measurements of D through first year sea ice grown in a laboratory setting, in an attempt to gauge the magnitude of D relative to other mechanisms of gas transfer in ice-covered regions of the ocean. We present measurements of the time evolution of dissolved gases in a well-mixed water bath overlain by a laboratory analogue of first year sea ice that is in contact with air of constant and known gas composition. Two gases, SF$_6$ and O$_2$, with diffusion coefficients that differ by a factor of 2 in water, were used to estimate gas diffusion. To our knowledge these are the first laboratory measurements of gas diffusion through sea ice, although the process is physically similar to gas diffusion through the unsaturated or vadose zone in soil. The results of these experiments and our interpretation are presented as follows: Section 2 reviews what is understood about the porosity and physical structure of sea ice that make it conducive to material transport. In Section 3, we describe the laboratory methods used to infer gas transport through columnar sea ice, based on the analysis of ice cores for bulk SF$_6$ concentration, salinity and the total (ϕ) and gas-filled (ϕ_D) porosity. Section 4 reports on the rate of O$_2$ and SF$_6$ diffusion and relates those results to the estimates of ϕ and ϕ_D. In Section 5, we attempt to constrain the processes encompassed within the bulk gas diffusion coefficient, including brine drainage and solubility partitioning between the gas and liquid phases. A simple model is used to simulate the effect of solubility partitioning and diffusion of gas through the liquid and gas-filled pore spaces, and to reproduce the trends observed in these tank experiments. We compare the magnitude of the diffusive gas flux with a prior estimate of sea to air gas flux through leads from Takahashi et al. (2009). Finally, Section 6 summarizes these results and discusses the range of their applicability.

2. The pore structure of sea ice

Sea ice is a porous medium with a crystal structure and a bulk composition that is distinct from freshwater ice (Golden et al., 2007). During seawater freezing, dissolved solutes (ions and gases) are segregated from the ice (Richardson, 1976) and become concentrated in the liquid near the freezing interface. Some debate persists as to whether segregation leads to an initial fractionation of solutes between the water and ice or whether drainage processes alone lead to desalination (Notz and Worster, 2009). As gases become supersaturated beneath growing ice, bubbles nucleate and are included along ice crystal boundaries (Bari and Hallett, 1974; Cox and Weeks, 1983). Sea ice is a het-

erogeneous medium on the microscale where brine inclusions range from 0.1 to 10 mm in length (Light et al., 2003) and air inclusions span a size distribution from 0.01 to 1 mm in first year sea ice (Light et al., 2003) to tens of millimetres as drained brine channels in multiyear hummock (Perovich and Gow, 1996). The brine pockets and brine channels together represent the total porosity, ϕ, with values in first year sea ice ranging from 2% to 40% by volume ($\phi = 0.02$ to 0.4) (Perovich and Gow, 1996).

Gas-filled pockets in first year sea ice typically result in ϕ_D values from 0.01 to 0.05 based on the state equations of Cox and Weeks (1983) and citations therein. In a laboratory sea ice experiment, vertical profiles of CO$_2$, O$_2$, N$_2$ and total gas content show that the vertical variability in gas concentration is significant with O$_2$ and N$_2$ exhibiting similar-shaped profiles, whereas CO$_2$ profiles are distinctly different, likely due to carbonate alkalinity precipitation (Tison et al., 2002). These authors propose that gas content in ice is determined not only by solubility and total gas pressure, but by current speed under the ice, which regulates the dimension of the solute diffusive boundary layer and produces greater bubble nucleation as the current increases. As the ice was warmed in their experiments, the profiles of O$_2$/N$_2$ demonstrate exchange at the ice/air interface as the ratio decreases away from O$_2$/N$_2$ = 0.56 (in water) towards O$_2$/N$_2$ = 0.27 (in air). However, surprisingly, the total gas content generally appeared to decrease as warming took place. Although air bubbles are found in freshwater ice (Craig and Hayward, 1987), the pore connectivity is significantly reduced and indeed the rate of gas diffusion through freshwater ice is $\sim$10^{-10} cm^2 s^{-1}, five orders of magnitude slower than molecular gas diffusion in water (Hemminsen, 1959).

The study of brine drainage has produced a well-established range in the liquid permeability of sea ice, which is similar to fine grain sand ($O(10^{-13})$ m^2), and decreases by an order of magnitude as ϕ decreases from 0.25 to 0.05 (Golden et al., 2007). Porosity is temperature-dependent and decreases exponentially in the temperature range between -2 and -5 °C, and then log linearly below -5 °C until a value of 0.05 is reached for ϕ at which point brine drainage is thought to virtually cease (Cox and Weeks, 1988). Golden et al. (2006) have established a theoretical upper bound for liquid permeability that reproduces this behaviour using cylindrical capillaries whose internal radii are representative of brine porosity. On larger scales, brine inclusions coalesce to brine drainage channels but the majority of these channels remain isolated from the bulk water until the onset of warming and melt (Cole and Schapiro, 1998).

3. Methods

3.1. Experimental design

A total of six sea ice formation experiments were conducted in a variable temperature cold room at the US Army Corps of
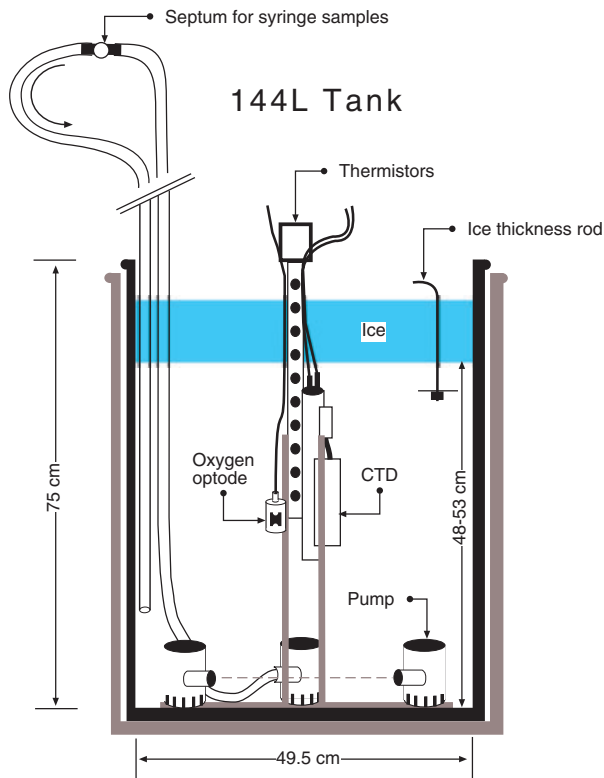
Fig. 1. Diagram showing instrument configuration in the 144L experimental tank.

Engineers Cold Regions Research and Engineering Lab (CR-REL) in Hanover, NH. During three of these experiments (Exps 1, 3 and 5), the bulk diffusion coefficient, D, was estimated under constant ice thickness conditions. Exps 2, 4 and 6 will not be reported here, but are included in a companion article (Loose et al., 2009). An insulated 144 L polypropylene drum ($d \times h = 49.2 \times 75$ cm) with a lid and rubber gasket was placed inside a constant temperature cold room to produce ice formation by cooling at the surface (Fig. 1). Salinity, temperature and pressure were measured using a CTD sonde (Seabird SBE 37SIP). Dissolved oxygen was measured using an oxygen optode (Aanderaa Data Instruments 3830). The optode computes the dissolved O_2 concentration in μmoles L^{-1} of freshwater. The resulting data was post-processed to correct for the saltwater effect on the optode measurement. Temperature was measured vertically from the air through the ice and into the water using a bar of 10 thermistors (YSI 44033) with 5 cm spacing. To produce a well-mixed condition within the tank, two bilge pumps (ITT Corporation Rule 360) were placed into the tank and oriented so that their jets impacted each other to maximize turbulence while minimizing circulation in the tank. A third bilge pump was used to continually circulate water through insulated Tygon tubing for discrete SF$_6$ sample collection, using a Tee-fitting with septum attachment to withdraw water.

Before each experiment, artificial seawater was prepared by mixing purified water (Milli-Q) with sea salt for aquariums (Spectrum Brands Instant Ocean) to achieve a salinity between 33 and 35 psu as verified with a conductivity probe. Artificial seawater was filtered through a 5-μm filter to remove any particulates in the mixture. Before introducing the water, the tank was cleaned with 10% bleach solution. All instruments and tubing introduced into the tank were also thoroughly cleaned and flushed with 10% bleach solution for at least 1 hr to minimize the growth of bacteria. The experimental sea ice tank was kept in a cold room with no interior light source to eliminate the possibility of algal growth and O_2 production. Fluorescent lights were turned on for less than 5 min several times a day to sample the air in the cold room and measure the ice thickness. An attempt was made to autoclave the seawater solution before an experiment. However, we observed the presence of a white powder in the autoclave vessel, indicating mineral precipitation during the autoclave cycle, which precluded the use of the autoclave for sterilizing the water for our experiments.

To initiate an experiment, the cold room was set to a temperature between -10 and -25 °C and the seawater bath was allowed to cool from an initial temperature of 26 °C. As the temperature decreased below 5 °C, air (N$_2$) was bubbled through the water bath for oxygen evasion (invasion), until the oxygen concentration was within 20% of complete saturation (depletion). Subsequently, ca. 10^{-7} moles of SF$_6$ were added as a concentrated solution dissolved in 5 mL of freshwater, and the solution was allowed to mix entirely. The volume of the 144 L tank was flushed through the pumps approximately every 3 min, so that complete mixing should take place in 15–20 min. The time evolution of the dissolved gas concentration beneath the ice was recorded and related to the established gas boundary conditions above and below the ice. O_2 was conditioned for gas evasion from the water during the first experiment (Exp. 1) by placing the lid on the tank, with a small opening to continuously flush the space between the ice and the lid (headspace) with pure N$_2$ gas throughout the duration of the experiment, thereby creating a volume of zero SF$_6$ and O_2 concentration above the ice. However, the lid also caused heat retention. To achieve colder ice surface temperatures during subsequent experiments (Exps 3 and 5), the lid was removed and O_2 was conditioned for gas invasion into the water.

Ice thickness was used to confirm steady-state ice conditions (neither freezing nor melting) and to calculate the water volume change in the tank. Subsequent to the formation of a consolidated ice cover, measurements of ice thickness were recorded daily using a 1/8 in. $\times$ 30 cm stainless steel rod with a flat plate attached to the bottom. By freezing the rod into the ice, the thickness was measured by pulling the rod upward until the plate contacted the bottom of the ice. Stainless steel has a greater thermal conductivity than ice, causing more rapid heat transfer and freezing along the perimeter of the steel rod. The effect of local freezing around the rod eliminates the possibility for 'gas

leakage' adjacent to the rod. The final ice thickness measurements were compared with ice cores extracted from the ice with a 3 in. diameter ice-coring tool at the end of the experiments. Ice thickness measurements were within 0.5 cm of the length of the ice cores.

After each experiment, two to six ice cores were collected for thin section micrography and solute analysis. Upon removal, the ice core for thin section micrography was placed in a sealed plastic bag and stored in a cold room at $-30\,°C$ for several days before preparing thin section slides. The ice core for solute analysis was immediately transferred to a $-14\,°C$ cold room, and vertical slices of 1.5–2 cm were cut using a band saw. The edges of the thin section were removed from each slice to produce a rectangular wedge ($2 \times 2 \times 7$ cm) of ice, which was placed in a 50 mL plastic syringe. Before replacing the syringe plunger, the syringe barrel was purged with ultra-high purity (99.999%) N_2 gas to remove all air. Positive gas pressure was maintained during plunger replacement, and venting N_2 from the syringe tip through a Luer lock fitting restored atmospheric pressure. The syringes were placed in a 26 $°C$ water bath and ice inside was allowed to melt and equilibrate with the headspace for 24–48 h. Melted ice core samples were analysed for SF_6 concentration, using the headspace method (Wanninkhof et al., 1987). Subsequently, the syringe plunger was removed to insert a conductivity meter (YSI Model 30) for salinity measurements. Ice core samples were not analysed for O_2 concentration, because analysis for O_2 using gas chromatography was not available at the time of the experiment.

3.2. SF_6 sampling and measurement

Water samples for SF_6 were collected using 50mL glass syringes and needles. Ten millilitres of water were drawn through a sep-

tum using a 16-gauge needle. To extract the SF_6 from the water, 30 mL of UHP N_2 was introduced to the syringe and vigorously shaken for 15 min (Wanninkhof et al., 1991). Samples were analysed using a gas chromatograph equipped with an electron capture detector (ECD) as described by Ho et al. (1997). With two gas standards and three sample volumes, a six-point calibration was used to account for non-linearity in the ECD response. Instrument drift was detected by measuring a gas standard near the range of sample concentration every five samples or four times a day, whichever came first. Duplicate samples were collected at each time interval and the average value was used except in cases where a contaminated sample was suspected. The standard error between replicates was approximately 2%. Water pressure in the tank was monitored using the pressure sensor on the CTD sonde. Atmospheric pressure was monitored with a pressure transducer (Omega Engineering 204). Prior to freeze-up of the tank, the water depth and atmospheric pressure were recorded, and the atmosphere-corrected tank pressure was monitored during ice growth. The difference between the initial pressure (P_0) in mb and the pressure at time t, P_t, is plotted in Fig. 2 for each of the three experiments. During ice growth, some water samples were not re-injected to compensate for the pressure increase caused by expansion. Ice formation in a confined vessel presses against the sides of the vessel, precluding the floe from achieving the natural freeboard prescribed by buoyancy. Once constant ice thickness was attained, the water pressure beneath the ice cover was regulated by reintroducing the volume of degassed water (10 mL) through the septum. The effect of ice growth can be observed as an increase in pressure in Fig. 2 (especially Exps 3 and 5) prior to the initiation of the diffusion experiments.

The measured gas concentration was corrected for the dilution effect of sampling by assuming that no appreciable amount of O_2
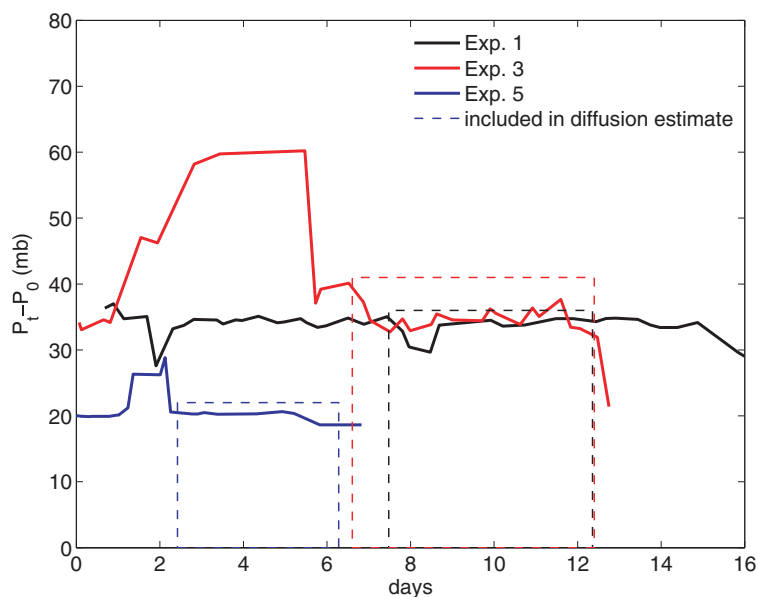

Fig. 2. Time series of the difference between the initial pressure (P_0) in the tank and the instantaneous pressure at time t (P_t) during each of the three experiments. The 'dashed' squares indicate the period during which the diffusion coefficients were estimated.

or SF$_6$ remained in the re-injected water sample. Over the course of an experiment, the amount of water removed and re-injected for sampling was 1–1.5 L, or less than 2% of the tank volume. At the time each SF$_6$ water sample was collected, a gas sample was collected from the cold room and from the headspace in the case of O$_2$ evasion, to establish the boundary condition above the ice. After thermal equilibration, gas samples of SF$_6$ were introduced to the GC in the same manner as water samples. In the cold room, the O$_2$ concentration was assumed to be atmospheric (20.95%) and O$_2$ concentration in the headspace was inferred by assuming that a negligible quantity of SF$_6$ in the headspace indicated that the O$_2$ concentration in the headspace was zero as well, implying that the flow of N$_2$ was sufficient to purge the headspace of all other gases.

3.3. Porosity estimates

Direct measurements of total gas content in ice cores taken from Exps 1 to 5 were made at the Laboratoire de Glaciologie of the Universitée Libre de Bruxelles (ULB) (Tison et al., 2002). An ice core from Exp. 3 was not available for analysis. The total gas content of an individual thin section is the sum of gas in non-wetted pore spaces and gas dissolved in brine within wetted pore spaces. ϕ_D is the difference between the total gas and the correction for gas in brine pockets (Tison et al., 2002). These measurements have shown that the thin section imagery produced in this study tended to overestimates the ice porosity so that a 'calibration' of the porosity from images is required to accurately estimate the total porosity. The following procedure was developed for calculating porosity during Exps. 1 and 5, and for estimating the porosity of Exp. 3.

The brine-filled porosity $(\phi - \phi_D)$ was determined using an equation of state for sea ice determined empirically (Frankenstein and Garner, 1967; Perovich and Gow, 1996)

$$\phi - \phi_D = S\left(0.0532 - 4.919/T\right), \tag{1}$$

where S can be estimated from the bulk salinity of sea ice in g kg^{-1} and T is the ice temperature in °C. Equation (1) gives the same result (within 4%) as the state equation derived by Cox and Weeks (1983). The total porosity, ϕ, for Exps 1 and 5 was thus estimated as the sum of the gas-filled porosity (ϕ_D) and the brine filled porosity resulting from the Frankenstein and Garner equation. The calculations of brine volume were then subtracted from the estimates of ϕ, derived from thin section micrographs for Exps 1 and 5. The resultant estimate of gas-filled porosity from micrograph $(\phi_{D,I}$, described in the next section) was plotted versus the measurements of ϕ_D from the ULB (Fig. 3), and a linear relationship was fitted to the data points, with an R^2 value of 0.61. The values of ϕ_D for Exp. 3 were estimated using the linear relationship in Fig. 3, and ϕ was reconstructed from the sum of ϕ_D and the brine volume. The individual values of ϕ and ϕ_D from thin sections, taken from each experiment, are displayed in Table 3.
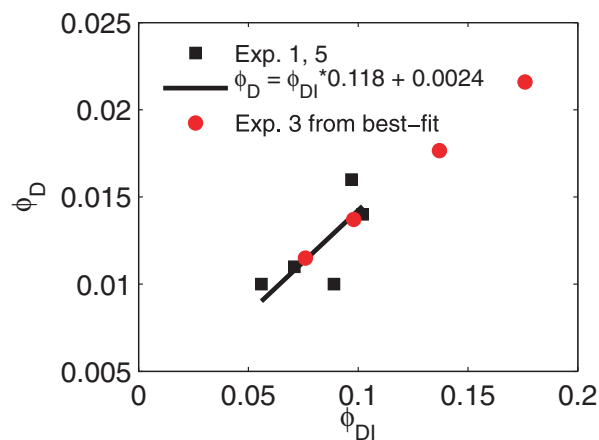

Fig. 3. Gas-filled porosity from image analysis (ϕ_{DI}) versus gas-filled porosity from air-content measurements on ice cores at the Laboratoire de Glaciologie of the Universitée Libre de Bruxelles (ϕ_D). The black line is a linear fit, and the estimated values of ϕ_D for Exp. 3 were produced by applying the fit ϕ_{DI} from Exp. 3.

3.4. Preparation and analysis of thin section micrographs

Thin sections were prepared in a cold room at −14 °C. The ice core was cut into ∼1.5–2 cm segments using a band saw and these segments were mounted onto glass plates by placing the glass plate and ice slice onto a hot plate to produce a thin lens of water between the slice and the glass (Gow et al., 1990, and references therein). A bead of freshwater was applied to the edges of the section to weld the thin section to the plate around the perimeter. Each glass-mounted segment was shaved with a microtome to a thickness between 1.4 and 1.8 mm that was deemed optimal for preserving the dimension of inclusions while minimizing the path length of the transmitted light. Still images of each section were photographed through a microscope (Leica MZ16), using transmitted light from an LED light source. The cold room temperature was set at the ice surface temperature from each experiment, to represent the ambient conditions during diffusion (e.g. −3.8 °C for Exp. 1, −11.8 °C for Exp. 3 and −7.5 °C for Exp. 5). Thin sections were stored at −30 °C, but were allowed to equilibrate to the imaging temperature for at least 2 hr before photographing. A mercury thermometer was used to confirm that thin sections remained at the cold room temperature while illuminated. At maximum magnification, the nominal pixel width is ca. 0.002 mm. However, the images used for analysis of inclusions were taken at a lesser magnification, approximately 0.009 mm. At this resolution, we estimate that features larger than 0.03 mm can be resolved.

Images of horizontal cross sections were analysed using an image analysis program (ImageJ: http://rsbweb.nih.gov/ij/). The dark features in transmitted-light images of sea ice represent inclusions within the ice. Gas inclusions generally appear darker (and more round) in aspect than brine inclusions, with a bright

spot in the centre; this is caused by the greater index of refraction between ice and air (Perovich and Gow, 1996). However, the distinction between gas and brine can be ambiguous in transmitted images. A threshold value of brightness was established to separate brine and gas inclusions, which appeared darker than 104 (out of 255). Anything lighter in the image was considered to be ice. In general, this approach tends to include grooves as brine pockets, although it is unclear whether these grooves are brine channels that have been excavated during microtoming or whether they were originally gas-filled (Light et al., 2003). Image analysis was performed on images of approximately 10 × 14 mm in size, and three to four images taken from different depths in each core.

3.5. Sources/sinks of O_2

To test for the presence of bacteria, 50 mL of tank water was drawn during Exp. 1 and centrifuged at 8400 × g for 15 min. A 200 μL aliquot was spread plated onto marine agar (synthetic seawater supplemented with 5 g L^{-1} peptone, 1 g L^{-1} yeast extract and 15 g L^{-1} agar at pH 7.8) and incubated at 25 °C for 48 h. The remaining sample was stained with 1.5 μL of a bacteria viability stain (LIVE/DEAD BacLight, Molecular Probes, Invitrogen, Carlsbad, CA) and a 10 μL aliquot was viewed with epifluorescent microscopy. Bacteria were not visible and no outgrowth was observed on the plate. Thin sections were then prepared for subsequent bacterial culture from two of

the ice cores collected during Exp. 3. The microtome blade was disinfected with isopropyl alcohol before shaving the samples. Sea ice cores were microtomed and immediately pressed onto marine agar plates and growth monitored over 48 hr at 25 °C. The first incubation resulted in growth of both bacteria and mold, however the mold was also detected on control plates set up in the cold room next to the microtome. In stark contrast, the second preparation produced no detectable growth. Discrepancy between the two samples may be explained by contamination (possibly from the microtome), inability of true psychrophiles (organisms that are suited to cold temperatures) to grow at the incubation temperature (25 °C), inability of microorganisms to utilize the media provided for growth, or sampling occurring at zones void of bacteria. In the initial core sectioning, only two of the five cores sampled showed substantial microbial growth.

4. Results

4.1. Gas concentrations and salinity in the tank

The temporal evolution of salinity, O_2 and SF$_6$ in the tank, all normalized by their maximum concentration (Fig. 4), reflect two distinct periods: growth of columnar ice and constant ice thickness. During ice growth, the solute concentration increases in the underlying water as a result of segregation from the ice matrix, which is described in more detail in Loose et al. (2009). Once steady ice thickness has been achieved, the residual drainage
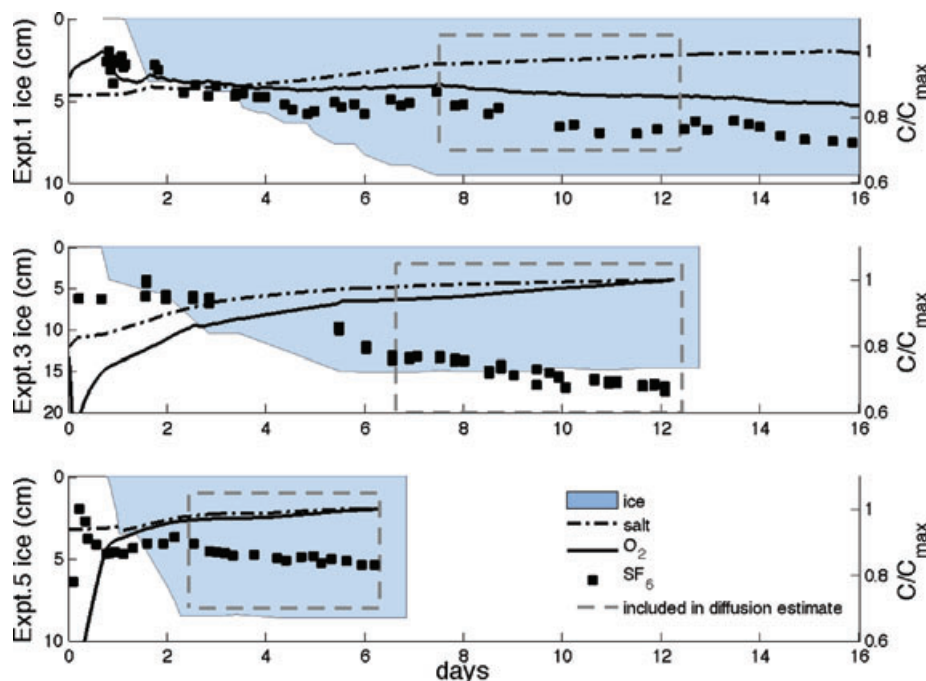
Fig. 4. Time series of aqueous O_2, SF$_6$ and salt concentration (C) normalized by their maximum values (C_{max}), over the course of Exp. 1, 3 and 5 (7–16 days). The blue filled regions indicate the ice thickness. The dashed boxes indicate the period of constant ice thickness, and relatively stable temperature conditions that were used to calculate the gas diffusion, D.

of brine produces only a small increase in salinity as compared to the change that occurred during ice growth, an effect that is observable in the slope of salinity in Fig. 4. The variation in pressure $P(t)$ in the tank was less than 5% from the reference pressure during all three experiments, except during the period of freezing when the pressure increased through down-growth of ice (Fig. 2). At the onset of steady ice thickness, the reference pressure was restored in the tank by removing small volumes of bulk water. Hereafter, the results and calculations that we describe correspond to the period of constant ice thickness indicated by a grey dashed line in Fig. 4. The net increase in the mass of salt was 0.63% per day for Exp. 1, 0.61% for Exp. 5 and 0.47% for Exp. 3. These results are consistent with the differences in ice surface temperature during each experiment: Exp. 1 was conducted at a mean ice-surface temperature of -3.8 °C, Exp. 3 at a temperature of -11.8 °C and Exp. 5 at -7.5 °C. Warmer ice is more permeable for liquids (Golden et al., 1998), potentially yielding a greater brine flux.

During the period of constant ice thickness, the changes in O_2 and SF_6 show nearly linear slopes during all three experiments. The total change in the normalized concentration were always less than 8% for SF_6 and less than 7% for O_2, indicating that the air–water concentration gradient changed very little during these periods. In such cases, the diffusive flux is nearly constant, producing a linear trend in the gas concentration. The average SF_6 concentration above the ice was less than 0.1 pmol kg^{-1} (we use units of aqueous concentration instead of partial gas pressure for consistency, assuming solubility equilibrium at the temperature and salinity in the bulk tank water) during all three experiments, or less than 0.0025% of the concentration beneath the ice. The SF_6 concentrations above the ice in each experiment are reported in Table 1.

4.2. SF_6 and salinity in ice cores

The mass balance of salt in the tank and in the ice is a useful comparison to the non-conservative behaviour of the gases. To calculate the salt balance, the bulk salinity of melted ice was multiplied by the liquid water equivalent of the ice. The final mass of salt in Table 1 is the sum of the salt content in the ice and salt in the tank just before ice cores were collected. For Exps 1 and 3, the difference between initial and final salinity was less than 1%, which we consider to be within the precision of the calculation. During Exp. 5, the difference between initial and final salt mass was 3%. We believe that this difference can be attributed to an underestimate of the bulk salinity in the ice. The volume of each ice core section used for salt and gas analysis was smaller than in previous cores, which caused difficulty in submerging the conductivity probe completely and would produce a lower salinity.

The vertical temperature profiles from the water through the ice to the air, in Fig. 5, depict the steady state temperature gradient from near -2 °C at the base of the ice to between -5

and -12 °C. These profiles are time-averages taken during the period of constant ice thickness. The temperature dependence of ice porosity leads to a vertically variable permeability in the ice, with the most impermeable layer existing somewhere near the ice/air interface. This variability can result in a 'C'-shaped salinity profile with two salinity maxima at the top and bottom of the ice (Cox and Weeks, 1983). High salinity is observed in Exps 1 and 3 near the ice/air interface, but the salinity profiles appear inverted in Exp. 5 (Fig. 5). No apparent skeletal layer was observed at the base of the ice cores, possibly it was not able to withstand the pump stirring, and thus the salinity profiles would appear truncated. One measurement of salinity from Exp. 5 at 0–1.5 cm is missing as the volume of melted ice was not sufficient to entirely submerge the conductivity probe.

The SF_6 concentration profiles in the ice, such as salinity, reflect the bulk concentration in the mass of melted ice from which the gas sample was extracted—the values have been normalized by the ambient concentration in the tank just before the ice cores were collected (C_{tank}). In contrast to the salinity profiles, the SF_6 concentration is greatest at the base of the ice, and decreases to the ice/air interface in each experiment. The maximum in SF_6 concentration occurred consistently at the ice/water interface. Furthermore, the SF_6 concentration in the ice layer next to the ice/water interface was higher than the ambient water concentration during Exps. 3 and 5. These values in excess of the water concentration indicate partitioning between the liquid and gas phases, with SF_6 accumulating in bubbles or gas pockets. This observation may indicate that gas inclusions communicate with brine inclusions.

4.3. Porosity estimates

A single horizontal thin section and a single vertical thin section from each of the diffusion experiments are displayed in Fig. 6. The directly illuminated horizontal thin sections in the first row of Fig. 6 depict both the liquid and gas-filled inclusions. The second row depicts the geometry of the pore spaces using a brightness threshold of 104 out of 255. By viewing the images through two sheets of polarizing paper-oriented perpendicular to each other, the change in crystal orientation between ice platelets causes a colour shift that highlights the location of the platelet boundaries (Fig. 6, rows 3 and 4). This perspective shows that some of the brine pockets and gas bubbles are oriented along, and are connected to, the boundaries between adjacent ice platelets, while others appear isolated or connected in only one location along the perimeter of the inclusion. A groove from the microtome is visible in the transmitted image depicted in Fig. 6. This feature was excluded from the surface area for image analysis.

The vertical estimates of ϕ and ϕ_D are listed in Table 2, together with the mean and standard deviation for each experiment. With the exception of 4.5–6 cm in Exp. 1 and 13–15.4 cm in Exp. 3, ϕ shows a decreasing trend from the ice/water interface to the ice/air interface, consistent with the decreasing

Table 1. Ambient conditions for water pressure in the tank, SF_6 concentration and air temperature above the ice, during the period of constant ice thickness

Ambient conditions	Exp. 1	Exp. 3	Exp. 5
Average water pressure (mb, absolute)	975.70	980.68	983.37
SD water pressure (mb, absolute)	1.25	1.06	0.72
Average SF_6 conc. above ice (pmol/kg)	0.006	0.105	0.004
SD SF_6 conc. above ice (pmol/kg)	0.008	0.457	0.003
Air temperature above ice (°C)	−4.5	−16.4	−13.2
Ice surface temperature (°C)	−3.8	−11.8	−7.5
Salt mass balance (ice and water)			
Initial salinity	35.23	35.60	34.80
Final salinity	39.60	43.25	37.43
Ice core salinity	3.78	5.84	6.58
Initial mass (g)	4177.50	4415.14	3915.41
Final mass (g)	4188.80	4458.35	3786.63
$\lvert dS \rvert$ (%)	0.27	0.98	3.29
SF_6 mass balance (ice and water)			
Onset of freezing (Julian day)	80.17	107.59	134.40
Time of ice core (Julian day)	95.45	120.68	140.10
SF_6 at onset of freeze (pmol kg^{-1})	38.30	2496.80	235.00
SF_6 at time of ice core (pmol kg^{-1})	28.87	1747.20	223.51
Initial water level (cm)	61.00	63.80	59.50
Ice thickness (cm)	9.50	14.50	8.50
Ice surface area (cm^2)	1943.90	1943.90	1943.90
Ice–water equivalent (L)	18.47	28.19	16.52
dV (L)	2.92	4.37	2.92
Volume before ice (L)	118.58	124.02	115.66
Volume below ice (L)	102.33	99.22	101.12
Initial mass, SF_6 (pmol)	4541.53	309655.18	27180.58
Final mass, SF_6: in water + in ice (pmol)	3226.15	228946.26	25649.35
dM	1315.38	80708.93	1531.24
dt (days)	15.28	13.09	5.70
dM/dt	86.09	6165.69	268.64
$D_{\text{ice+water mass balance}}$ (10^{-5} cm^2 s^{-1})	13.0	19.7	5.2

Notes: SF_6 is expressed in units of pmol/kg, assuming solubility equilibrium. The term $D_{\text{ice+water mass balance}}$ is an estimate of D taken from the total mass balance of SF_6 in the ice and in the tank water, and they are included as 'diamonds' in Fig. 7.

temperature along this same trajectory. The trend in ϕ_D is less clear, but appears to be opposite of the total porosity, increasing from the ice/water interface to the ice/air interface. By entering the measurements of salinity from the ice cores and time-averaged ice temperature (Fig. 5) into eq. (1), the brine volumes were estimated as 0.066 and 0.065, and 0.040, respectively, for Exps 1, 5 and 3. The estimates of ϕ_D from air content measurements (and calibrated image analysis for Exp. 3) increase from 0.013 ($\pm$ 15%) in Exp. 1 and 0.014 ($\pm$ 28%) in Exp. 5 to 0.019 ($\pm$ 31%) in Exp. 3. The individual estimates of brine volume and ϕ_D sum to ϕ, whose average values were 0.079 ($\pm$16%), 0.079 ($\pm$20%) and 0.061 ($\pm$10%), respectively for experiments 1, 5 and 3 (Fig. 6 and Table 3). The 1σ deviation was used as a

measure of the error in successive estimates of porosity, although much of the variability between images may also be attributed to the changing vertical structure of porosity within the ice.

5. Discussion

5.1. Ice porosity

The estimates of ϕ from this study ranged between 0.061 and 0.079, which is on low end of the range of sea ice permeability: 0.02–0.4; (Perovich and Gow, 1996, #205). The values in this study are only slightly above the liquid permeability threshold of $\phi = 0.05$ (Golden et al., 2007, #113), however, the gas
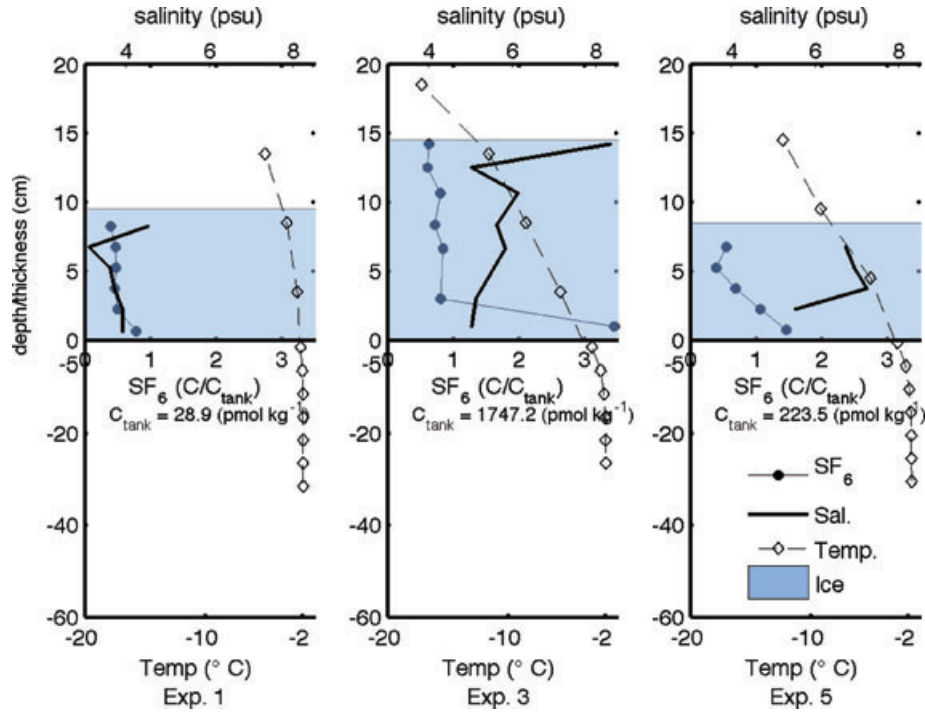
Fig. 5. Profiles of temperature, salinity and SF$_6$ showing the gradients from the tank through the ice to the air (or pure N$_2$ in the case of Exp. 1). These profiles were taken from 3 in. ice cores extracted at the end of each diffusion measurement. Zero on the vertical axis indicates the ice/water interface, and the SF$_6$ concentration (C_{tank}) represents the water concentration at the time that the ice cores were extracted.

permeability threshold for sea ice has yet to be determined. The estimates of total gas content (ϕ_D) in these experiments ranged between 0.013 and 0.019, which is also on the low end of ϕ_D for first year sea ice cited by Cox and Weeks (1983) (ϕ_D from 0.01 to 0.05). However, ϕ_D from this study exceeded the values measured during the experiments of Tison et al. (2002): ϕ_D from ca. 0.003 to 0.017 (based on bulk ice salinity of 930 kg m^{-3}). The bulk salinities that were observed from the ice cores were low (e.g. 4–6 psu, averaged vertically) in comparison to a more typical range of 8–10 psu (Tison et al., 2002). This may be an indication that brine drainage was more extensive in these experiments, possibly due to the apparent absence of a skeletal layer at the base of the ice, which tends to retain a greater portion of salinity or brine. As previously noted, the pump stirring in the tank may have caused the skeletal layer to erode.

5.2. Bulk gas diffusion through the ice

The mixture of liquid- and gas-filled pore spaces found in the soil vadose zone is descriptively similar to the pore composition inside sea ice. Whereas some differences, such as water density and capillary pressure may exist between the two, gas transport in the vadose zone provides a well-developed theoretical and empirical framework that can be used as a point of departure for the interpretation of gas transport through sea ice (Vogel, 1997; Aachib et al., 2004; Moldrup et al., 2004; Tick et al., 2007). The

dusty gas model (DGM), based on gas kinetic theory, is generally considered a better approximation of differential gas diffusion (Webb and Pruess, 2003). However, most empirical estimates of the effective diffusion coefficient are based on Fick's second law, and the differences between the models become less significant as the liquid filled porosity increases, such as in sea ice. In soils, D normalized by the free air gas diffusion coefficient (D_o), is related empirically ϕ_D and ϕ, that is $D/D_o \propto f(\phi_D, \phi)$ (Golden et al., 2006; Kawamoto et al., 2006).

To estimate D, Fick's first law was applied directly to the change in gas concentration during a small interval in time, as opposed to using a curve fit procedure with Fick's second law (Weeks et al., 1982). This is justifiable considering the nearly linear trend observed in the O$_2$ and SF$_6$ time series (Fig. 4). The approach is similar to the thin film model for gas exchange; the gas flux in moles per second, is

$$F = -\frac{D}{z_{ice}}(C - C_{EQ})A, \qquad (2)$$

where C is the dissolved gas concentration in the water beneath the ice, C_{EQ} is the gas concentration above the ice, using solubility equilibrium at -2 °C and 35 psu, z_{ice} is the ice thickness and A is the cross-section of the tank. F can be estimated from the time-rate of change of the gas concentration beneath the ice: $F = dC/dt \cdot Ah$, where h is the water depth beneath the ice. If the ice thickness, tank volume and surface remain constant, the equation can be integrated for the diffusion coefficient as
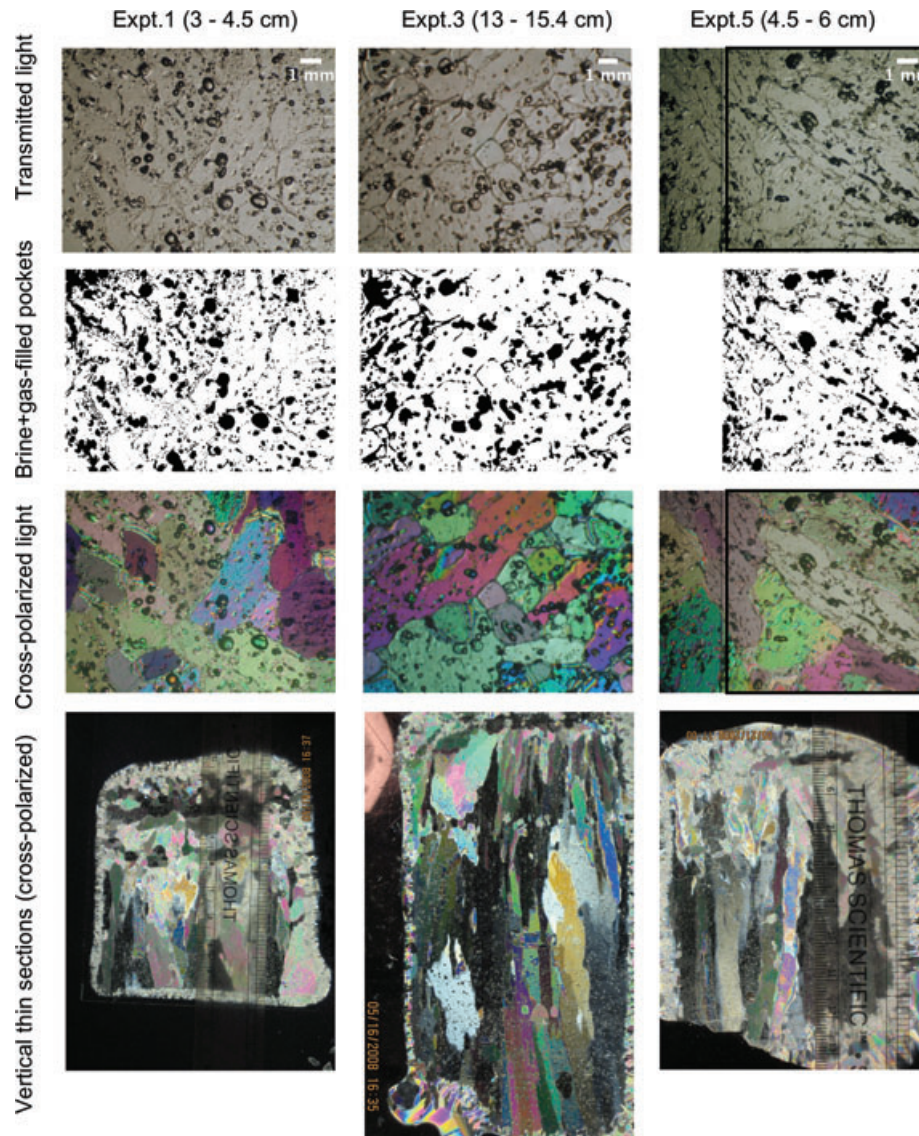
Fig. 6. Horizontal and vertical thin section micrography of ice from Exps. 1, 3 and 5. The second row shows the geometry of the brine+gas-filled pockets. Using cross-polarizers (rows 3 and 4), the ice platelet boundaries are illuminated to illustrate their connectivity with a portion of the liquid and gas filled inclusions, and to illustrate the orientation of platelet boundaries in the vertical thin sections (row 4).

Table 2. Estimates of gas-filled and total porosity, ϕ, taken from air and brine content measurements (Exps. 1 and 5) and from air content and thin section micrographs (Exp. 3)

Exp. 5			Exp. 1			Exp. 3		
Core depth (cm)	ϕ_D	ϕ	Core depth (cm)	ϕ_D	ϕ	Core depth (cm)	ϕ_D	ϕ
0–1.5 cm	0.016	0.098	0–1.3 cm	0.013	0.089	0–2 cm	0.011	0.069
3–4.5 cm	0.010	0.074	3–4.5 cm	0.011	0.064	2–4 cm	0.014	0.062
4.5–6 cm	0.016	0.067	4.5–6 cm	0.014	0.083	7.25–9.6 cm	0.019	0.054
			7.5–9 cm	N/A	N/A	13–15.4 cm	0.023	0.060
SD	0.004	0.016	*SD*	0.002	0.013	*SD*	0.005	0.006
Mean	0.014	0.079	Mean	0.013	0.079	Mean	0.017	0.061

Table 3. Estimates of ϕ, ϕ_D, D_{SF_6} and D_{O_2}, during each experiment. The error estimates in ϕ and ϕ_D comes from 1σ deviation in thin section measurements of ϕ and ϕ_D from Table 2

	Exp. 5	Exp. 1	Exp. 3
Gas-filled porosity (ϕ_D)	0.014 ($\pm$28%)	0.013 ($\pm$15%)	0.017 ($\pm$31%)
Total porosity (ϕ)	0.079 ($\pm$20%)	0.079 ($\pm$16%)	0.061 ($\pm$ 0%)
D_{SF_6} (10^{-5} cm^2 s^{-1})	8 ($\pm$38%)	12 ($\pm$48%)	20 ($\pm$34%)
D_{O_2} (10^{-5} cm^2 s^{-1})	3 ($\pm$30%)	6 ($\pm$72%)	3 ($\pm$22%)

follows:

$$D = \frac{hz_{ice}}{(t_f - t_i)} \ln\left[\frac{C_i - C_{EQ}}{C_f - C_{EQ}}\right], \tag{3}$$

where subscripts "f" and "i" indicate the final and initial state during the period over which the estimate is being performed. The high temporal resolution O_2 samples were block-averaged to a consistent time interval of 2 hr for each experiment and a 24-hr running average was applied to the time series. D was estimated as the average of these values during the period of constant ice thickness. The error in D was estimated as the 1σ deviation from this average. A 24-hr running average was also used to smooth the SF_6 measurements. Because of the coarser temporal resolution of the SF_6 measurement, a linear slope was fit to the natural log of the concentration, to determine D. In this case, the root-mean square of the residuals was used as an estimate of the error in D. The individual estimates of D_{O_2} and D_{SF_6} in each experiment are plotted as a function of total porosity in Fig. 7 (left panel), and shown in Table 3. The values of D_{SF_6} could indicate that as total porosity increases, the effective gas phase diffusion also increases, however these differences are within the errors of the measurements. At the minimum measured value of

$\phi = 0.061$, D_{SF_6} was 20 ($\pm$34%) $\times$ 10^{-5} cm^2 s^{-1} and D_{O_2} was 3 ($\pm$22%) $\times$ 10^{-5} cm^2 s^{-1}. When ϕ increased to 0.079 (during Exp. 5), D_{SF_6} decreased to 8 ($\pm$38%) $\times$ 10^{-5} cm^2 s^{-1} and D_{O_2} did not change, detectably (3 $\pm$ 30% $\times$ 10^{-5} cm^2 s^{-1}). At the same value of ϕ during Exp. 1, D_{SF_6} and D_{O_2} were 12 ($\pm$48%) and 6 ($\pm$72%) $\times$ 10^{-5} cm^2 s^{-1}, respectively. Based on these results, there was no apparent trend between the bulk diffusion coefficient and the total porosity, over the range of porosities that were produced in these experiments. However, it merits pointing out that the greatest value of D_{SF_6} coincided with the largest value of gas-filled porosity; when ϕ_D was 0.019, D_{SF_6} was 20 $\times$ 10^{-5} cm^2 s^{-1}.

As mentioned earlier, the first known field measurements of gas diffusion in sea ice come from Gosink et al. (1976), who report a value of D_{SF_6} of ca. 4 $\times$ 10^{-6} cm^2 s^{-1} at $-15\,°$C. In the same study, D_{CO_2}, the diffusion coefficient of CO_2, was found to be 9 $\times$ 10^{-4} cm^2 s^{-1} at $-7\,°$C (the conversion from cm^2 s^{-1} to cm^2 s^{-1} atm^{-1} is P/RT from the ideal gas law). This overall range of D using CO_2 and SF_6 spans two orders of magnitude between over a temperature range of -7 to $-15\,°$C. Part of this range can be attributed to difference in the rate of molecular diffusion, which is 2.4 times larger for CO_2 than
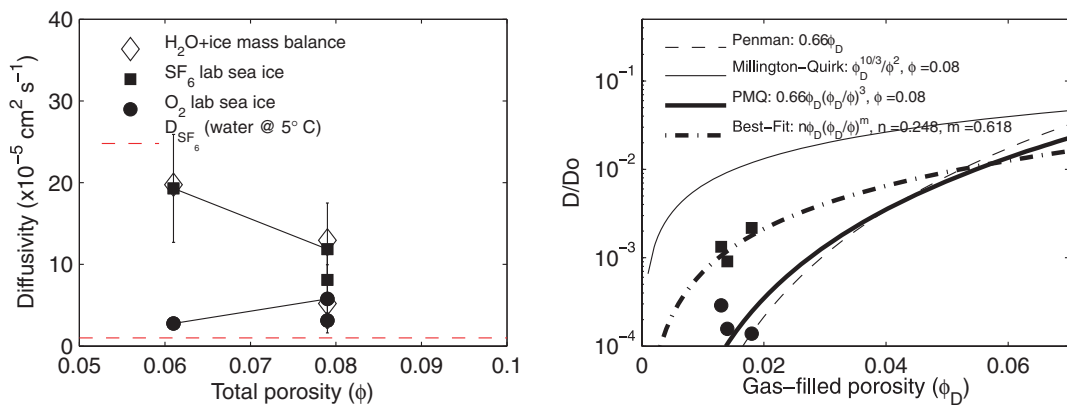

Fig. 7. Left panel: The relationship between D and ϕ, in laboratory sea ice. For reference, the water diffusion of SF_6 (King and Saltzman, 1995) at 5 °C is plotted. The right panel depicts the same estimates of D, normalized by the free air gas diffusion, D_o. The curves represent three common soil–gas diffusion models; the Penman model, Millington–Quirk model and the generalized Penman–Millington–Quirk (PMQ) empirical model, that relate D to the gas-filled and total porosity for undisturbed soils (Kawamoto et al., 2006). The curves were calculated using the value of $\phi = 0.079$ from these experiments. The curves indicated by 'dash-dots' are the best-fit to the measured values of D_{SF_6}, ϕ and ϕ_D using the two parameter, PMQ model: $D/D_o = n\phi_D(\phi_D/\phi)^m$, where the least-squares fit yielded $n = 0.047$ and $m = -0.424$.

for SF$_6$. Nonetheless, much of this range is likely a result of the temperature-driven change in sea ice porosity, which gives some interesting insights into the variation that can occur as a result of temperature-driven changes in the ice porosity. The estimate of D_{SF_6} from this study is a factor of 10 larger than what was measured by Gosink et al. (1976) at an ice surface temperature of $-11.8\,^\circ$C, which seems to further indicate the potential for large changes in molecular diffusion over relatively small changes in the ice temperature. Further comparison between the two studies is difficult, without more information on the ice type/porosity.

It is somewhat unexpected that, in this study, regardless of the direction of the O$_2$ concentration gradient (favouring invasion or evasion), the total change in O$_2$ was 20–45% less than that for SF$_6$. The diffusion coefficient of O$_2$ in freshwater ($\sim 2 \times 10^{-5}$ cm^2 s^{-1}) and in air (~ 0.2 cm^2 s^{-1}) is more than twice that of SF$_6$ in freshwater ($\sim 0.7 \times 10^{-5}$ cm^2 s^{-1}) and in air (~ 0.09 cm^2 s^{-1}) (O'Brien and Hyslop, 1977; King and Saltzman, 1995; Werner and Hhener, 2003). However, the solubility of O$_2$ is four times greater in water than that of SF$_6$ (Weiss, 1970; Bullister et al., 2002): the Bunsen solubility coefficient (V_{gas}/V_{water}) is 0.038 for O$_2$ and 0.009 for SF$_6$ at 0 $^\circ$C salinity of 35. The more rapid depletion of SF$_6$ in these experiments may reflect the combined effect of solubility and diffusion on the net gas transport (Weeks et al., 1982). This result is considered in more detail later (Section 5.4).

The right panel of Fig. 7 depicts D normalized by D_o in comparison with three empirical models of gas phase diffusion in undisturbed soils: (1) the Penman model, $D/D_o = 0.66\phi_D$, (2) the Millington–Quirk model, $D/D_o = \phi_D^{10/3}/\phi^2$ and (3) the general Penman–Millington–Quirk (PMQ) model, $D/D_o = 0.66\phi_D(\phi_D/\phi)^3$ (Moldrup et al., 2004; Kawamoto et al., 2006). These models are meant to capture the effects of a tortuous flow path and other retardation processes that change as the ratio of gas-filled porosity to total porosity changes. At a fixed value of $\phi = 0.079$ and the range of ϕ_D in these experiments, our results fall between the predictions of the PMQ and the Millington–Quirk models, however these two trends predict values of bulk gas diffusion that differ by two orders of magnitude, indicating a wide range of possible values.

We suspect that tortuosity, a measure of length in the mean free diffusion path divided by the chord between two points (Zalca et al., 2003), is significantly greater in sea ice than in soils. This is because some fraction of the bubble inclusion in the ice matrix may represent 'dead-ends' or may be sealed off entirely from the porous microstructure of the ice. Examining the shape and distribution of the features that compose ϕ_D (Fig. 6), it is possible to observe bubble inclusions that appear isolated from the brine channels or are connected in only one location. To explore the tendency in D/D_o implied by our estimates of D, we can use the two-parameter fit model of PMQ, $D/D_o = n\phi_D(\phi_D/\phi)^m$ and the three estimates of D_{SF_6}, ϕ and ϕ_D to determine values for n and m in sea ice, using a least-squares fit (the natural log transform of the Millington–Quirk equation gives an equation

that is linear in $\ln(n)$ and m.) The results, plotted as dot-dash lines in Fig. 7, depict a slightly shallower dependency between D_{SF_6} and ϕ_D, as compared with the soil diffusion models, which may be accurate if a significant fraction of the gas-filled pore space is isolated or dead-ended from the overall pore structure of the sea ice. The values of n and m were 0.047 and -0.424, respectively. However, it is important to recognize that this best-fit trend is poorly constrained over the range of ϕ_D that can exist in first year sea ice (0.01–0.05), given the narrow range of ϕ_D that were reproduced in these experiments. As indicated earlier, there is no consistent trend in the rate of diffusion of both SF$_6$ and O$_2$. Furthermore, if these empirical relationships between bulk diffusion and the permeability were sufficient to account for the processes affecting diffusion, we would expect that $(D/D_o)_{SF_6}$ and $(D/D_o)_{O_2}$ would fall along the same curve of ϕ and ϕ_D. This indicates that other processes are also affecting the observed diffusion rate.

In soils, D represents the net effect of advection in the liquid phase, sorption onto soil grains, counter-diffusion from water vapour transport during evaporation, solubility partitioning between phases and molecular diffusion in both the liquid and gas phase. In ice, we expect brine convection, along with liquid and gas phase diffusion to be the most relevant factors. Although sorption of gas molecules onto the ice crystal structure may take place, that process is beyond the capacity of this study to evaluate. In the sections that follow we will attempt to distinguish the effects of residual brine drainage from solubility partitioning, which both contribute to multiphase diffusion, and attempt to constrain the relative importance of those factors in determining net gas transport as an explanation for the diffusion results that we have reported earlier.

5.3. Gas transport via residual brine drainage

The profiles of SF$_6$ concentration in the ice give some indication of the vertically variable permeability (Fig. 5). At the base where the ice is warmest, it produces the greatest permeability followed by a progressive decrease towards the colder ice/air interface. The elevated SF$_6$ concentrations at the ice/water interface indicate exchange with the tank water and partitioning of gas from the brine to the gas-filled pockets. Further up in the ice, the gas concentrations rapidly become depleted indicating that despite restricted permeability, a diffusive pathway exists between the gas phase in the ice and the overlying gas space (the vertical change in ϕ_D is not large enough to account for this difference in SF$_6$ concentration). The thin section micrographs show interfacial contact between brine and gas pockets. If the matrix of brine and bubbles are close to solubility equilibrium, very little gas will remain in the brine. For example, the concentration of SF$_6$ (O$_2$) in the brine would be less than 0.6% (0.2%) of the tank concentration, in each of the three experiments (please refer to Appendix for an explanation of this calculation). Based on the salt balance, the brine flux amounted to less than 3% of the tank

volume for all three experiments (Appendix), implying a 3% dilution of both SF_6 and O_2 in the tank.

Dilution of the tank concentration by brine drainage would enhance the total change in gas and thus enhance the magnitude of D, during gas evasion. For gas invasion, brine drainage would suppress the change in O_2 concentration, creating a smaller apparent magnitude in D. In this sense, gas invasion and evasion cannot be considered equivalent means to measure the bulk value of D. However, degassing of brine is not expected to be a significant factor affecting mixed-layer gas budgets, especially for CO_2 because brine volumes are small and CO_2 is a small fraction of total inorganic carbon. Based on this calculation, brine drainage would act to enhance D_{SF_6} compared to D_{O_2}, but a 3% dilution is not sufficient to account for the differences that were observed between the two apparent diffusion coefficients. The set-up of these experiments did not permit proper separation of brine drainage from bulk gas diffusion, but this simple estimate reveals that brine drainage was not the primary factor affecting gas transport in these experiments.

5.4. Solubility partitioning and gas-phase diffusion

Given that the diffusion rate of O_2 is twice the diffusion rate of SF_6 in both water and air, it is somewhat counterintuitive that our observations of D through the ice were greater for SF_6 than for O_2. This difference implies that solubility partitioning between the liquid and gas phase may be an important factor because O_2 is four times more soluble in water, than SF_6. Because gas diffusion is four orders of magnitude faster than aqueous diffusion, the ability of SF_6 to partition to the gas phase more readily would provide it a more rapid diffusive pathway. To test the effect of solubility, we have conducted a very simplistic simulation wherein a large aqueous reservoir (the tank) is connected with a small gas reservoir (the gas pockets distributed vertically in the ice), and the two reservoirs are initially in solubility equilibrium. The aqueous reservoir is connected to the atmosphere by a liquid diffusive pathway and the gas reservoir is connected to the atmosphere by a gas diffusive pathway (see schematic with boundary conditions in Fig. 8). The diffusion equation,

$$\frac{\partial C}{\partial t} - D\frac{\partial^2 C}{\partial z^2} = 0 \qquad (4)$$

is solved simultaneously for both pathways using an implicit numerical solution. The boundary condition at the ice/air interface is applied as a constant concentration (C_{atm}) in the final element of the mesh. The boundary condition at the ice/water interface compares the gas concentration in the liquid (C) and gas (X) reservoirs; if they are not in solubility equilibrium, a quantity of molar mass (dM) is transferred between them,

$$dM(t) = V_g \left(X(t) - \frac{C(t)}{H} \right) \left(\frac{P}{RT} \right) \qquad (5)$$

$dM > 0$ causes a flux from the gas reservoir to the liquid reservoir and $dM < 0$ produces a flux in the opposite direction. Initially, the liquid and gas reservoirs are in solubility equilibrium. The term V_g represents the gas volume, and P is assumed to be at atmospheric pressure (1013 mb). V_g is used as a tunable parameter, and it is iteratively adjusted to bring the results of the simulation in line with the observations.

The simulation was computed for a period of 10 days, which encompasses the time of the laboratory diffusion estimates. This simple simulation reproduces similar trends to our observations of O_2 and SF_6. The aqueous SF_6 concentration decreases more rapidly than O_2 as it preferentially partitions into the gas phase, and moves along this diffusive pathway. By applying the particular conditions of each experiment (e.g. boundary concentrations and ice thickness) and adjusting the gas volume iteratively, the simulation can be tuned to reasonably approximate the specific trends observed in each experiment, both for gas invasion and gas evasion (Fig. 8, right side). The gas reservoir volume necessary for equilibration was 6.5 cm^3 for Exp. 1 and 5.2 cm^3 for Exp. 3. These volumes are small in comparison to the gas content in the ice: 230 cm^3 in Exp. 1 and 502 cm^3 for Exp. 3, so that V_g is between 3% and 1% of the total porosity in the ice at a given instant in time, which implies that only a small amount of the gas content in the ice represents a purely gas-diffusive pathway. This simulation is an oversimplification of the interaction between the gas pockets, the brine and the bulk water, however it offers some insight into the pathways of gas transfer; e.g. that (1) gas-filled inclusions are able to exchange gas with brine and that (2) a gas diffusive pathway along crystal grain boundaries, or a transient pathway produced as brine drains and displaces gas volumes by buoyancy may participate in the bulk diffusion rate. Gas-phase diffusion along grain boundaries was previously postulated by Gosink et al. (1976). This result is also implied by the gas concentration profiles in the sea ice that become progressively depleted in SF_6 towards the ice/air interface.

5.5. Anomalous O_2 consumption

The presence of psychrophilic bacteria can be a source of O_2 consumption in sea ice, but our bacterial cultures have not determined conclusively whether measurable quantities of bacteria were present in these experiments. However, we can attempt to establish the order of magnitude that respiring psychrophyles might have had on these experiments by referring to literature values of bacterial biomass in sea ice and estimates of their respiration rate. In his review article on psychrophylic bacteria, Morita (1975) stipulates that respiration rate decreases with temperature, for example from 348 μL per mg of cell protein per day at 15 °C to 168 μL per mg of cell protein per day at 4 °C. In midwinter sea ice from the Weddell Sea, Helmke and Horst (1995) observed bacterial biomass between 2 and 158 mg C m^{-3}, with a median value of 3.2 mg C m^{-3}, and Kottmeier and Sullivan (1990) report values of 77 mg C m^{-3} on average
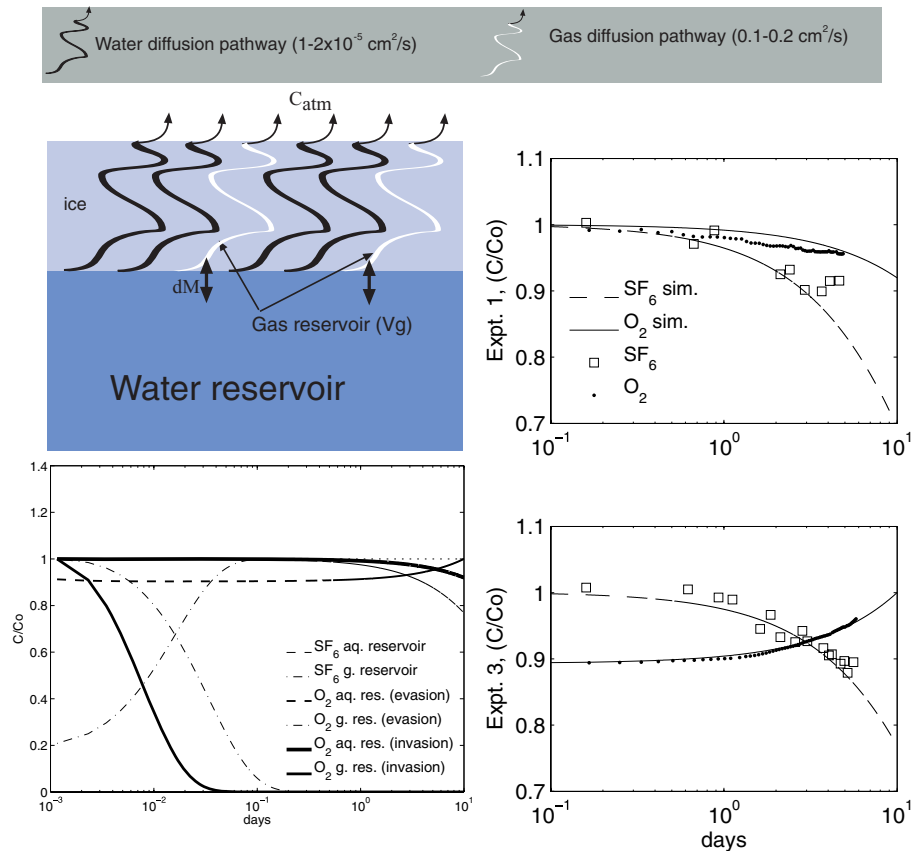
Fig. 8. Modelling scenario of separate gas and liquid diffusive pathways through the ice. Brine as a liquid in the ice provides a water diffusion pathway from the water reservoir to the air. The water reservoir is also in contact with gas bubbles in the ice, potentially providing a gas-diffusive pathway. The left panel depicts the time scales of exchange as the water reservoir and gas bubbles both equilibrate via diffusion. The right panels depict the aqueous concentration time series from Exps 1 to 3, together with model simulations of the same experiments.

in springtime Antarctic sea ice. If the molecular weight of protein can be approximated by the general formula for amino acid (NH$_2$–CH–COOH), then the conversion from bacterial carbon to bacterial cell protein is ca. 3.1. Although, the temperature of the sea ice in this study did not exceed −2 °C, the respiration rate at 4 °C reported by Morita (1975) can be used as an upper limit, which yields respiration rates between 0.0005 and 0.033 mL O$_2$ L^{-1} day^{-1}, using the range in biomass from Helmke and Horst (1995). In 10 days (a duration similar to the diffusion experiments), the consumption of 0.33 mL O$_2$ would be less than 3% of the O$_2$ consumption necessary to suppress the time rate of change of O$_2$ below that observed for SF$_6$. For example, respiration would have had to suppress an increase of 13 mL of O$_2$ in the 100 L tank, during the 6 days of constant ice thickness during Exp. 1.

While it is possible that the smaller values of D_{O_2} may have been affected by bacterial respiration, we think that this effect, if present, was small in comparison to the solubility partitioning within the ice. Admittedly, we have not been able to constrain the bacterial biomass in these experiments, however it is likely that, given the effort to suppress their growth, they would not have

been present in concentrations as great as in their natural habitat, for example Antarctic sea ice. Finally it is worth noting that had psychrophiles been present in sufficient quantity to affect the O$_2$ concentration, the effect should have amplified the decrease in O$_2$ during gas evasion in Exp. 1 (producing D_{O_2} greater than D_{SF_6}) and suppressed the increase in O$_2$ during gas invasion in Exps 3 and 5 (producing D_{O_2} less than D_{SF_6}, as observed). Instead, the rate of change of the O$_2$ concentration was consistently smaller than SF$_6$, indicating no significant difference in behaviour between Exp. 1 and Exps 3 and 5.

5.6. Diffusive flux versus flux through leads

To bring the magnitude of D and the diffusive flux into perspective, we have performed a simple comparison with an existing estimate of the gas transport pathway through leads and open water. Takahashi et al. (2009) estimated the gas exchange in the seasonal ice zone of the Southern Ocean. The air–sea gas flux from that study is, $F_{Gex} = \text{Tr } \Delta p CO_2$, where Tr is the gas transfer coefficient in g-C m^{-2} μatm^{-1} month^{-1}, and $\Delta p CO_2$ is the sea–air difference in CO$_2$ partial pressure. Those authors report
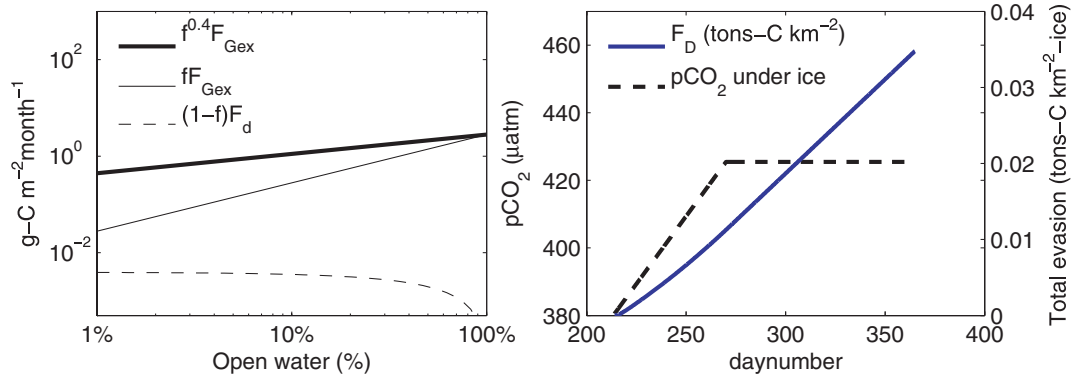
Fig. 9. Left panel: The diffusive flux, of CO_2 (F_d) assuming $D_{CO_2} = 2.4 \times 10^{-4}$ cm^2 s^{-1}, based on this study, compared with the gas-exchange flux (F_{Gex}) through leads and open water estimated by (Takahashi et al., 2009). Both fluxes assume a sea–air pCO_2 difference of 40 μatm. F_{Gex} is scaled linearly by the fraction of open water, f, and F_d by the fraction of ice ($1 - f$). At $f < 0.01$, $F_d(1 - f)$ is still five times smaller than fF_{Gex}. Right panel: Using the seasonal increase in pCO_2 beneath sea ice, estimated by Takahashi et al. (2009) ($pCO_2 = 0.802 \times$ days + 208.9), the diffusion equation is used to estimate the cumulative flux per km^2 of ice.

a sea–air pCO_2 difference of up to 40 μatm, based on measurements of pCO_2 beneath the Southern Ocean sea ice pack, and a value of Tr = 0.07, producing $F_{Gex} = 2.8$ g-C m^{-2} month^{-1}, given 100% open water. To scale this flux in the presence of sea ice, Takahashi et al. (2009) reduced the gas flux by a proportion equivalent to the fraction, f, of open water in a unit area. At $f = 0.1$, F_{Gex} would be 0.28 g-C m^{-2} month^{-1}.

By comparison, the diffusive flux of CO_2 can be estimated by scaling D_{SF_6} by the Schmidt number ratio of SF_6 and CO_2 at -2 °C (to the power of -0.5) to produce $D_{CO_2} = 2.4 \times 10^{-4}$ cm^2 s^{-1}, so that the diffusive flux of CO_2, F_D, through 50 cm of sea ice, using the same ΔpCO_2 is 0.004 g-C m^{-2} month^{-1}, two orders of magnitude smaller than the gas exchange flux at 10% open water. This difference is depicted graphically in Fig. 9 (left panel), where F_{Gex} is scaled linearly by f and by $f^{0.4}$ in accordance with the power-law tendency observed by Loose et al. (2009) and F_D is scaled by (1-f), the fraction of ice-covered water. At $f = 0.01$, F_{Gex} is still five times greater than F_D. If we use the seasonal evolution of pCO_2 from Takahashi et al. (2009) ($pCO_2 = 0.802 \times$ days + 208.9), and then maintain a constant value of 425 μatm from day 270 until the end of the year, the total flux is 0.035 Tons-C m^{-2} during the season, which is small in comparison to the fluxes estimated by Takahashi et al. (2009) (see their Figure 16, panel D). Given these estimates of the gas diffusion rate through sea ice, the seasonal diffusive flux from the Southern Ocean mixed layer through sea ice to the atmosphere appears small in comparison with gas transfer through leads, even when the surface area of leads is less than 1% of the total ice pack.

6. Summary and conclusions

These laboratory measurements were intended as a reproduction of first-year sea ice under temperature conditions that resemble winter and early spring, when the pack is most consolidated and

the ice porosity is at its smallest. Based on the bulk salinity and total gas content measurements, the total porosity observed in these experiments ranged within $0.061 < \phi < 0.079$ and the gas-filled porosity ranged between $0.013 < \phi_D < 0.019$, which are consistent with the low end of the porosity range for cold first-year sea ice. The decrease in temperature from the ice/water interface to the ice/air interface reflect the physical conditions typically associated with late winter/early spring, when the air temperature is colder than the water temperature.

The effective gas diffusion rates through sea ice observed in this study were 1.3×10^{-4} cm^2 s^{-1} ($\pm 40\%$) for SF_6 and 3.9×10^{-5} cm^2 s^{-1} ($\pm 41\%$) for O_2. We were only successful in varying the ice porosity over a narrow range (0.061–0.079) and it was not possible to ascertain a dependency between either ϕ or ϕ_D and the diffusion coefficient over this range. Instead, these experiments give some idea of the magnitude of D just above the liquid permeability threshold of $\phi = 0.05$. In sea ice, increased porosity can lead to greater residual brine drainage, but the effect of gas-transport in brine depends on gas partitioning processes within the ice. Therefore the porosity–permeability relationship may not be as straightforward as it is in soils where water motion is more often perpendicular to direction of vertical gas diffusion. Although the effective D for both O_2 and SF_6 was much closer to the aqueous diffusion rate ($\sim 10^{-5}$ cm^2 s^{-1}) than to the gaseous diffusion rate (~ 0.1 cm^2 s^{-1}), the preferential partitioning of SF_6 into gas-filled pore spaces within the ice, appeared to produce a greater bulk diffusion rate for SF_6 as compared to O_2.

In aggregate, this study and the results of Gosink et al. (1976) tend to support the prior assumption that gas ventilation of the mixed-layer takes place primarily through fractures in the ice, even when the open water fraction is small, for example Takahashi et al. (2009), Stephens and Keeling (2000), Toggweiler (1999), and others. However, turbulence production beneath ice and in the vicinity of leads may not be dominated by wind-driven mixing. In this case, the magnitude of gas exchange through

leads is not simply a linear function of the open water area, implying that the gas flux would not follow the wind-speed scaling that is used for the open ocean.

As ice warms, it is well established that much of the brine will drain, leaving an air-filled pore space. As ice porosity increases into spring, the gas permeability is expected to increase substantially and indeed this process is supported by field measurements of authigenic gas production and gas fluxes above the surface of the sea ice in springtime when $\Delta p CO_2$ can approach $-350\,\mu$atm (Delille et al., 2007) and DMS can be two orders of magnitude higher in the brine than in the atmosphere (Zemmelink et al., 2008). Under these conditions, gas diffusion through snow and melting sea ice may be much more rapid than the rates that were observed in this study.

7. Acknowledgements

8. Appendix A:

A. 1. Brine drainage calculations

Although the concentration of gas was not measured directly in the bubble and brine inclusions, we can estimate the gas transport through residual brine drainage by assuming that the brine and gas pockets are close to solubility equilibrium with each other and by using the estimates of ϕ_D and ϕ, together with an estimate of the brine flux from the bulk ice salinity and the observed change in salinity in the tank. If gas exists only within the voids and brine filled inclusions, the molar mass of gas is

$$M_{bulk} = V_{Ice} C_{bulk} \rho_{Ice} = \left[X_G V_G \left(\frac{P}{RT} \right) + C_{br} V_{br} \rho_{br} \right], \quad (A.1)$$

where X_G is the partial gas pressure in the gas-filled inclusions, V_G and V_{br} are the gas and brine volumes, respectively, and ρ_{Br} is the brine density. Solubility equilibrium between the brine and bubbles means, $X_G H = C_{br}$. H is the gas solubility coefficient, P, R and T are the pressure, ideal gas constant and gas temperature. The gas-filled and brine-filled porosity from the image analysis are $\phi_D = V_G / V_{Ice}$ and $\phi - \phi_D = V_{br} / V_{Ice}$, respectively. Substituting these into A.1 and rearranging, the concentration of

gas in the brine, C_{br}, can be estimated as

$$C_{br} = \frac{V_{Ice} C_{bulk}}{\frac{\phi_D}{H} \left(\frac{P}{RT} \right) + \phi_L \rho_{br}}, \qquad (A.2)$$

where C_{bulk} is the measured gas concentration in the melted ice core, or the vertical average of the profiles in Fig. 5. This approach assumes for simplicity that no gas has escaped the ice. The total residual brine drainage during the period of constant ice thickness is approximated assuming no volume change in the tank, that is any flux of brine into the tank must be accompanied by a vertical flux of water into the ice. In nature, the brine flux could induce water upwelling into the ice or produce a greater gas-filled porosity, which effectively would lower the density of the ice. However, in the tank the ice is frozen to the sides and so it cannot ride higher as a result of decreased density. The total volume flux of brine is

$$F_{br} = \frac{dDSV_T \rho_{sw}}{S_{br} \rho_{br} - S_T^I \rho_{sw}}, \qquad (A.3)$$

where $dS = S_T^F - S_T^I$, that is the difference between the final and the initial salinity in the tank, ρ_{sw} is the seawater density and V_T is the tank volume.

Based on these calculations, the residual brine drainage during Exps 1, 3 and 5 would have exchanged 2%, 0.7% and 0.9% of the tank volume, respectively. The concentration of SF$_6$ in the brine would have been less than 0.3% of that observed in the ambient water concentration, implying that the SF$_6$ flux due to residual brine drainage would be less than 0.01% of the mass in the tank for all three experiments. This calculation can be performed for O$_2$ with the additional assumption that the ratio of O$_2$ to SF$_6$ in the brine is the same as it was initially in the water before ice formation began. Under this assumption, the O$_2$ concentrations in brine were less than 0.3% of the ambient water concentration during Exps 1, 3 and 5, respectively. Again, because the gas concentration in the brine is practically zero, the effect of brine drainage would be to dilute the ambient water by an amount equivalent to the brine drainage, just as with SF$_6$.

References

Aachib, M., Mbonimpa, M. and Aubertin, M. 2004. Measurement and prediction of the oxygen diffusion coefficient in unsaturated media, with applications to soil covers. *Water Air Soil Pollut.* **156**, 163–193.

Bari, S. A. and Hallett, J. 1974. Nucleation and growth of bubbles at an ice-water interface. *J. Glaciol.* **13**, 489–520.

Bullister, J., Wisegarver, D. P. and Menzia, F. A. 2002. The solubility of sulfur hexafluoride in water and seawater. *Deep-Sea Res. Part A— Oceanogr. Res. Papers* **49**, 175–187.

Cole, D. and Schapiro, L. H. 1998. Observations of brine drainage networks and microstructure of first-year sea ice. *J. Geophys. Res.* **103**, 21739–21750.

Cox, G. F. N. and Weeks, W. F. 1983. Equations for determining the gas and brine volumes in sea-ice samples. *J. Glaciol.* **29**, 306–316.

Cox, G. F. N. and Weeks, W. F. 1988. Numerical simulations of the profile properties of undeformed first-year sea ice during the growth season. *J. Geophys. Res.* **93**, 12449–12460.

Craig, H. and Hayward, T. 1987. Oxygen supersaturation in the ocean: biological versus physical contributions. *Science* **235**, 199–202.

Delille, B., Jourdain, B., Borges, A. V., Tison, J.-L. and Delille, D. 2007. Biogas (CO_2, O_2, dimethylsulfide) dynamics in spring Antarctic fast ice. *Limnol. Oceanogr.* **52**, 1367–1379.

Frankenstein, G. E. and Garner, R. 1967. Equations for determining the brine volume of sea ice from $-0.5\ ^{\circ}C$ to $-22.9\ ^{\circ}C$. *J. Glaciol.* **6**, 943–944.

Golden, K. M., Ackley, S. F. and Lytle, V. I. 1998. The percolation phase transition in sea ice. *Science* **282**, 2238–2241.

Golden, K. M., Heaton, A. L., Eicken, H. and Lytle, V. I. 2006. Void bounds for fluid transport in sea ice. *Mech. Mater.* **38**, 801–817.

Golden, K. M., Eicken, H., Heaton, A. L., Miner, J., Pringle, D. J. and co-authors. 2007. Thermal evolution of permeability and microstructure in sea ice. *Geophys. Res. Lett.* **34**, doi: 10.1029/2007GL030447.

Gosink, T. A., Pearson, J. G. and Kelly, J. J. 1976. Gas movement through sea-ice. *Nature* **263**, 41–42.

Gow, A. J., Meese, D. A., Perovich, D. K. and Tucker III, W. B. 1990. The anatomy of a freezing lead. *J. Geophys. Res.* **95**, 18221–18232.

Helmke, E. and Horst, W. 1995. Bacteria in sea ice and underlying water of the eastern Weddell Sea in midwinter. *Marine Ecol. Progress Ser.* **117**, 269–287.

Hemminsen, E. 1959. Permeation of gases through ice. *Tellus* **11**, 355–359.

Ho, D. T., Bliven, L., Wanninkhof, R. and Schlosser, P. 1997. The effect of rain on air-water gas exchange. *Tellus* **49B**, 149–158.

Kawamoto, K., Moldrup, P., Schjonning, P., Iversen, B. V., Rolston, D. E. and co-authors. 2006. Gas transport parameters in the vadose zone: gas diffusivity in field and lysimeter soil Profiles. *Vadose Zone J.* **5**, 1194–1204.

King, D. B. and Saltzman, E. S. 1995. Measurement of the diffusion coefficient of sulfur hexafluoride in water. *J. Geophys. Res.* **100**, 7083–7088.

Kottmeier, S. T. and Sullivan, C. W. 1990. Bacterial biomass and production in pack ice of Antarctic marginal ice edge zones. *Deep-Sea Res.* **37**, 1311–1330.

Light, B., Maykut, G. A. and Grenfell, T. C. 2003. Effects of temperature on the microstructure of first-year Arctic sea ice. *J. Geophys. Res.* **108**, doi: 10.1029/2001JC000887.

Loose, B., McGillis, W. R., Schlosser, P., Perovich, D. and Takahashi, T. 2009. The effects of freezing, growth and ice cover on gas transport processes in laboratory seawater experiments. *Geophys. Res. Lett.* **36**, doi: 10.1029/2008GL036318.

Moldrup, P., Olesen, T., Yoshikawa, S., Komatsu, T. and Rolston, D. E. 2004. Three-porosity model for predicting the gas diffusion coefficient in undisturbed soil. *Soil Sci. Soc. Am. J.* **68**, 750–759.

Morita, P. J. 1975. Psychrophylic bacteria. *Bacteriol. Rev.* **39**, 144–167.

Notz, D. and Worster, M. G. 2009. Desalination processes of sea ice revisited. *J. Geophys. Res.* **114**, doi: 10.1029/2008JC004885.

O'Brien, R. N. and Hyslop, W. F. 1977. A laser interferometric study of the diffusion of O_2, N_2, H_2 and Ar into water. *Can. J. Chem.* **55**, 1415–1421.

Papadimitriou, S., Kennedy, H., Kattner, G., Dieckmann, G. S. and Thomas, D. N. 2003. Experimental evidence for carbonate precipitation and CO_2 degassing during ice formation. *Geochimica et Cosmochimica Acta* **68**, 1749–1761.

Perovich, D. K. and Gow, A., J. 1996. A quantitative description of sea ice inclusions. *J. Geophys. Res.* **101**, 18327–18343.

Richardson, C. 1976. Phase relationships in sea ice as a function of temperature. *J. Glaciol.* **17**, 507–519.

Stephens, B. B. and Keeling, R. F. 2000. The influence of Antarctic sea ice on glacial-interglacial CO_2 variations. *Nature* **404**, 171–174.

Takahashi, T., Sutherland, S. C., Wanninkhof, R., Sweeney, C., Feely, R. A. and co-authors. 2009. Climatological mean and decadal change in surface ocean pCO_2, and net sea-air CO_2 flux over the global oceans. *Deep-Sea Res. Part II* **56**, 554–577.

Tick, G. R., McColl, C. M., Yolcubal, I. and Brusseau, M. L. 2007. Gas-phase diffusive tracer test for the in-situ measurement of tortuosity in the vadose zone. *Water Air Soil Pollut.* **184**, 355–362.

Tison, J.-L., Haas, C., Gowing, M. M., Sleewaegen, S. and Bernard, A. 2002. Tank study of physico-chemical controls on gas content and composition during growth of young sea ice. *J. Glaciol.* **48**, 177–191.

Toggweiler, J. R. 1999. Variation of atmospheric CO_2 by ventilation of the ocean's deepest water. *Paleoceanography* **14**, 572–588.

Vogel, H. J. 1997. Morphological determination of pore connectivity as a function of pore size using serial sections. *Eur. J. Soil Sci.* **48**, 365–377.

Wanninkhof, R., Ledwell, J. R., Broecker, W. S. and Hamilton, M. 1987. Gas exchange on Mono Lake and Crowley Lake, California. *J. Geophys. Res.* **92**, 14567–14580.

Wanninkhof, R., Ledwell, J. R. and Watson, A. J. 1991. Analysis of sulfur hexafluoride in seawater. *J. Geophys. Res.* **96**, 8733–8740.

Webb, S. W. and Pruess, K. 2003. The use of Fick's Law for modeling trace gas diffusion in porous media. *Transport Porous Media* **51**, 327–341.

Weeks, E. P., Earp, D., E. and Thompson, G. M. 1982. Use of atmospheric fluorocarbons F-11 and F-12 to determine the diffusion parameters of the unsaturated zone in the Southern High Plains of Texas. *Water Resources Res.* **18**, 1365–1378.

Weiss, R. F. 1970. The solubility of nitrogen, oxygen and argon in water and seawater. *Deep-Sea Res.* **17**, 721–735.

Werner, D. and Hhener, P. 2003. In situ method to measure effective and sorption-affected gas-phase diffusion coefficients in soils. *Environ. Sci. Technol.* **37**, 2502–2510.

Zalca, J. M., Reyes, S. C. and Iglesia, E. 2003. Monte-Carlo simulations of surface and gas phase diffusion in complex porous structures. *Chem. Eng. Sci.* **58**, 4605–4617.

Zemmelink, H. J., Dacey, J. W. H., Houghton, L., Hintsa, E. J. and Liss, P. S. 2008. Dimethylsulfide emissions over the multi-year ice of the western Weddell Sea. *Geophys. Res. Lett.* **35**, doi: 10.1029/2007GL031847.